ASJET

Al-Salam Journal for Engineering and Technology
Journal Homepage:
http://journal.alsalam.edu.iq/index.php/ajest
e-ISSN: 2790-4822 p-ISSN: 2958-0862

Microstructural and optical studies of La_2O_3 thin films prepared using pulsed laser deposition technique

Hussian Fakhry[1], Mohammed RASHEED[1]*, Odai N. Salman[1] and Raid A. Ismail[1]

[1]Applied Sciences Department, University of Technology- Iraq, Baghdad 10066, Iraq.

*Corresponding Author: Mohammed RASHEED

DOI: https://doi.org/10.55145/ajest.2026.05.01.002
Received August 2025; Accepted November 2025; Available online Febuary 2026

ABSTRACT: Lanthanum oxide (La_2O_3) thin films were successfully synthesized by the pulsed laser deposition (PLD) technique using a sintered La_2O_3 target prepared with a PVA binder. The structural, morphological, vibrational, and optical characteristics were systematically examined to evaluate their suitability for optoelectronic applications. X-ray diffraction confirmed a polycrystalline hexagonal A-type La_2O_3 structure with average crystallite sizes ranging from 20–30 nm and lattice parameters a = 3.94 Å, c = 6.13 Å. Atomic force microscopy revealed a compact granular surface with uniform topography (Sa = 30.17 nm, Sq = 38.34 nm), indicating homogeneous grain growth. FTIR and Raman spectra identified the fundamental La–O stretching vibrations at ~550–600 cm^{-1}, confirming phase purity and the absence of hydroxyl or carbonaceous impurities. Optical characterization demonstrated high transparency (~74 % in the visible range) and strong UV absorption, with a direct optical band gap of 3.81 eV. The extinction coefficient decreased from 5×10^{-13} to 1×10^{-13} across the visible region, highlighting low optical losses. The integration of structural, morphological, and optical analyses establishes a clear correlation between PLD parameters and film quality. The obtained results underscore the potential of PLD-grown La_2O_3 films as high-k dielectrics, UV-transparent layers, and thermally stable coatings for advanced optoelectronic and photonic devices.

Keywords: La_2O_3, XRD, AFM, Raman, FTIR

1. INTRODUCTION

Lanthanum oxide (La_2O_3) is a rare-earth sesquioxide that has drawn significant attention due to its high dielectric constant (~27), wide optical band gap (>5 eV), and excellent thermal and chemical stability, making it a promising material for optoelectronic and microelectronic applications [1-3]. These characteristics have led to its utilization as a high-k dielectric in complementary metal–oxide–semiconductor (CMOS) devices [4], protective coatings for optical components [5], and active layers in ultraviolet (UV) photodetectors [6]. Its low phonon energy also minimizes non-radiative losses, which enhances optical emission efficiency in photonic devices [7].

Various deposition techniques, including electron-beam evaporation [8], sol–gel [9], sputtering [10], atomic layer deposition (ALD) [11], and pulsed laser deposition (PLD) [12,13], have been investigated to fabricate La_2O_3 thin films. Among these, PLD stands out for its ability to preserve target stoichiometry, provide precise control over thickness, and yield films with excellent adhesion and purity [14]. The process involves focusing high-energy laser pulses onto a solid target to generate a plasma plume that condenses on the substrate, enabling the formation of high-quality oxide films. Previous studies have shown that deposition parameters such as laser fluence [15], substrate temperature [16], and ambient gas pressure [17] directly influence the structural, optical, and electrical properties of La_2O_3 films, which confirms the need for optimized processing routes.

Despite La_2O_3's promising physical and chemical characteristics, current research still lacks a comprehensive understanding of how PLD deposition parameters affect its microstructure, surface morphology, and optical behavior. Most previous works have been limited to chemically prepared or sputtered films, often analyzing either structural or

*Corresponding author: rasheed.mohammed40@yahoo.com

optical aspects in isolation. Furthermore, detailed correlations between the crystallographic features, surface roughness, and optical transparency of PLD-grown La_2O_3 films have rarely been reported. This knowledge gap constrains the effective design of La_2O_3-based layers for high-performance optoelectronic and dielectric applications.

In this context, the present work focuses on the fabrication and multi-technique characterization of La_2O_3 thin films deposited on fluorine-doped tin oxide (FTO) substrates using the PLD technique under controlled conditions. The La_2O_3 target was prepared from high-purity powder using a polyvinyl alcohol (PVA) binder, followed by sintering to ensure mechanical stability and stoichiometric consistency during ablation. The study systematically investigates the structural, morphological, vibrational, and optical properties of the resulting films using XRD, AFM, FTIR, Raman, and UV–Vis spectroscopy, thereby establishing a complete structure–property relationship. The measured optical band gap, surface roughness, and crystalline parameters are correlated to assess film quality and performance.

The novelty of this work lies in its integrated analytical approach and its focus on high-purity PLD-deposited La_2O_3 films, bridging the gap between fundamental material characterization and practical optoelectronic applications. By combining detailed microstructural, vibrational, and optical analyses, this study contributes new insight into how PLD parameters govern film uniformity, crystallinity, and transparency. The findings offer valuable guidance for optimizing La_2O_3-based thin films in transparent electronics, UV photonics, and dielectric device architectures.

limitations and future research directions: Although the pulsed laser deposition (PLD) technique successfully produced high-quality La_2O_3 thin films with uniform morphology and excellent optical transparency, several limitations were identified in the present study. First, the deposition was carried out at room temperature without substrate heating, which can restrict crystalline ordering and lead to partial amorphous content. Enhanced crystallinity could be achieved through substrate heating or post-annealing treatments in controlled oxygen environments. Second, the work focused mainly on structural, morphological, and optical characterization, while electrical and dielectric measurements—essential for evaluating the material's performance in microelectronic devices—were not performed. Including such analyses would provide deeper insight into charge transport, dielectric constant, and leakage behavior. Third, PLD, although advantageous for stoichiometric transfer and purity, is limited in scalability compared with industrial deposition routes such as sputtering or atomic layer deposition, which can handle large-area substrates. Furthermore, only one set of deposition parameters (700 mJ laser fluence, 2.5 cm target–substrate distance, 6 Hz repetition rate) was used, and no systematic optimization was conducted to explore parameter effects on film properties.

Future research should therefore focus on optimizing key deposition variables—such as laser fluence, repetition rate, and ambient oxygen pressure—to achieve superior crystallinity and smoother surfaces. Introducing substrate heating or performing post-annealing could further improve phase stability and reduce lattice defects. Complementary electrical and dielectric studies are also recommended to evaluate the films for high-k and transparent electronic applications. In addition, controlled doping with transition-metal or rare-earth elements (e.g., Cu, Co, or Ce) may allow fine-tuning of the optical band gap and dielectric behavior. Finally, comparative studies between PLD and scalable deposition techniques could help establish the most effective route for integrating La_2O_3 thin films into next-generation optoelectronic and photonic devices.

In this paper, La_2O_3 thin films were deposited via pulsed laser deposition under optimized conditions and characterized.

2. Materials and methods

2.1 Preparation of PVA Binder

Polyvinyl alcohol (PVA) was used as a binder to enhance the mechanical stability of the pressed La_2O_3 pellets. Specifically, 1 g of PVA resin powder (Fig. 1) was dissolved in 10 mL of distilled water under continuous magnetic stirring at 65 °C (Fig. 2). The heating and stirring were maintained for approximately 30 minutes to ensure complete dissolution of the polymer, resulting in a homogenous 10 wt.% PVA resin binder solution. This work addresses such challenges by carefully selecting laser fluence (700 mJ), pulse count (700 pulses), and target–substrate distance (2.5 cm) to ensure uniform and adherent La_2O_3 film deposition.

FIGURE 1 Polyvinyl alcohol (PVA) resin powder used for binder preparation

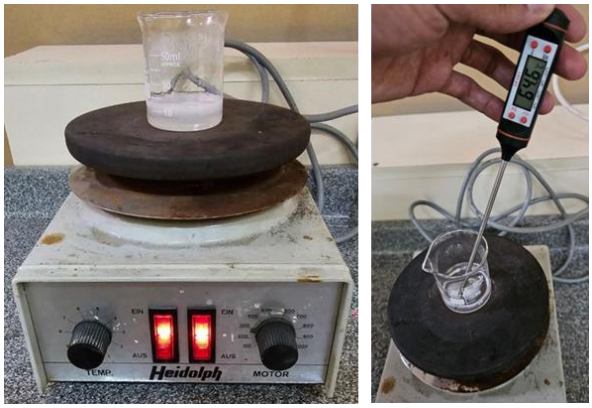

FIGURE 2 Magnetic stirrer utilized for dissolving PVA at 65 °C

2.2 Pelletization of La_2O_3 Target

To prepare the La_2O_3 pellet target, 0.2 mL of the previously prepared PVA binder was mixed with 2 g of high-purity lanthanum oxide (La_2O_3) powder using an agate mortar and pestle. The manual mixing process ensured uniform distribution of the binder and facilitated better bonding between the powder particles during pressing. The homogenized mixture was then placed into a stainless-steel mold and pressed at a uniaxial pressure of 1 MPa (equivalent to 10 tons) for 5 minutes using a hydraulic press (Fig. 3). This process yielded a green body pellet with a diameter of approximately 0.8 cm and a thickness of 0.6 cm (Fig. 4). The pellets were subsequently sintered in an electric furnace at 400 °C for 2 hours and 30 minutes, ensuring gradual heating to reach steady temperature conditions and achieve mechanical integrity.

FIGURE 3 Hydraulic press applying 1 MPa (10 ton) pressure for pellet formation

FIGURE 4 Prepared La_2O_3 pellet before deposition

2.3 Pulsed Laser Deposition (PLD) of La_2O_3 Films

Thin films of La_2O_3 were deposited using a pulsed laser deposition (PLD) system equipped with an Nd:YAG laser operating at a wavelength of 532 nm, pulse energy of 700 mJ, and a repetition rate of 6 Hz. The laser beam was focused through a 6 mm focal length lens, achieving a fluence of 12.50 J/cm². The beam was directed at the pellet target positioned inside a stainless-steel vacuum chamber at a 45° incidence angle (Fig. 5). The chamber was maintained at a base pressure of 10^{-2} torr and a room temperature of 14 °C.

During ablation, a visible plasma plume containing ablated atoms and ions was generated and deposited onto the substrate positioned at a distance of 2.5 cm from the target. The deposition process consisted of 700 laser pulses.

FIGURE 5 Pulsed laser deposition (PLD) system showing target and substrate configuration in the vacuum chamber

2.4 Substrate Preparation

Fluorine-doped tin oxide (FTO)-coated glass substrates (TCO30-10/LI, Solaronix SA) with dimensions 100 × 100 × 3 mm and sheet resistance of 10 Ω/sq were used. The FTO glass was cut into 1.5 × 2 cm pieces using a precision glass cutter. To ensure optimal film adhesion and surface cleanliness, the substrates were ultrasonically cleaned sequentially in ethanol (10 minutes), acetone (10 minutes), and deionized water (10 minutes). The cleaned substrates were dried using lint-free cigarette paper and then fixed to glass slides with double-sided adhesive tape for mounting in the PLD substrate holder (Fig. 6).

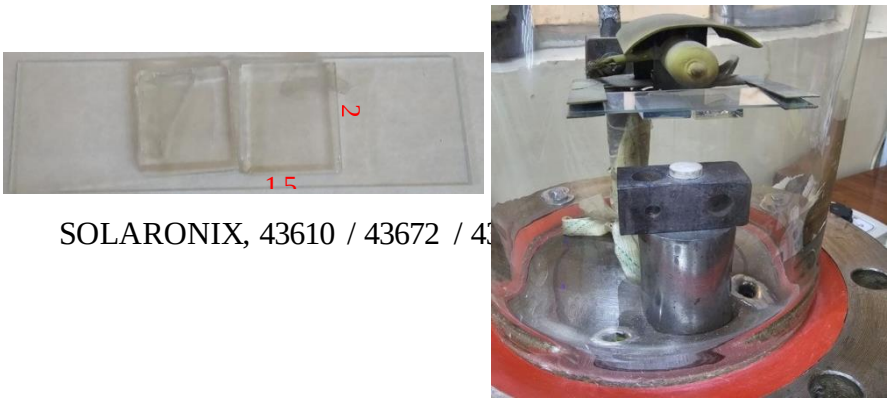

FIGURE 6 Cleaned FTO substrates fixed on glass slides and positioned in the PLD vacuum chamber

The thickness of the La_2O_3 thin films was determined using cross-sectional atomic force microscopy (AFM). A fine scratch was made on the film surface to expose the underlying FTO substrate, and the AFM tip scanned perpendicularly across the step edge. The height difference between the exposed substrate and the film surface in the topographic profile represented the film thickness. This approach also enabled simultaneous evaluation of surface roughness and uniformity with nanometer-scale precision, confirming homogeneous deposition. The measured La_2O_3 layer thickness was 126.4 nm, while the underlying FTO layer thickness was approximately 300 nm.

3. Results

3.1 AFM analysis

The atomic force microscopy (AFM) image in Fig. 7 presents the surface morphology of the La_2O_3 thin film fabricated via pulsed laser deposition (PLD) over a 10.5 × 10.5 µm² scan area. The surface features exhibit a densely packed grain structure with irregularly shaped agglomerates, indicating a polycrystalline nature. The grains appear as bright regions in the topographic map, corresponding to higher elevations, while darker areas represent lower surface valleys. This granular texture reflects the nucleation and growth mechanisms during PLD, where adatoms arriving at the substrate surface form islands that coalesce into continuous films.

The surface roughness analysis yields an arithmetic average roughness (Sa) of 30.17 nm and a root mean square roughness (Sq) of 38.34 nm. The relatively close values of Sa and Sq suggest a uniform roughness distribution without extreme height outliers. Such moderate roughness can enhance surface–substrate adhesion in multilayer device architectures, while still maintaining acceptable optical quality for applications requiring transparency. The observed surface topography suggests columnar grain growth, which is common in oxide films deposited under vacuum without additional surface smoothing treatments.

The uniform distribution of grain clusters and the absence of large voids or cracks indicate good film continuity, a key factor for electrical insulation and dielectric applications. The surface morphology could also influence light scattering and, consequently, the optical transmittance of the films. The presence of nanoscale peaks and valleys can increase surface area, which is beneficial in certain catalytic or sensing applications.

The AFM analysis confirms that the PLD-grown La_2O_3 thin film possesses a homogenous and well-packed granular structure with moderate surface roughness, making it potentially suitable for applications in dielectric layers, transparent electronics, and optoelectronic devices where both structural stability and controlled surface morphology are essential.

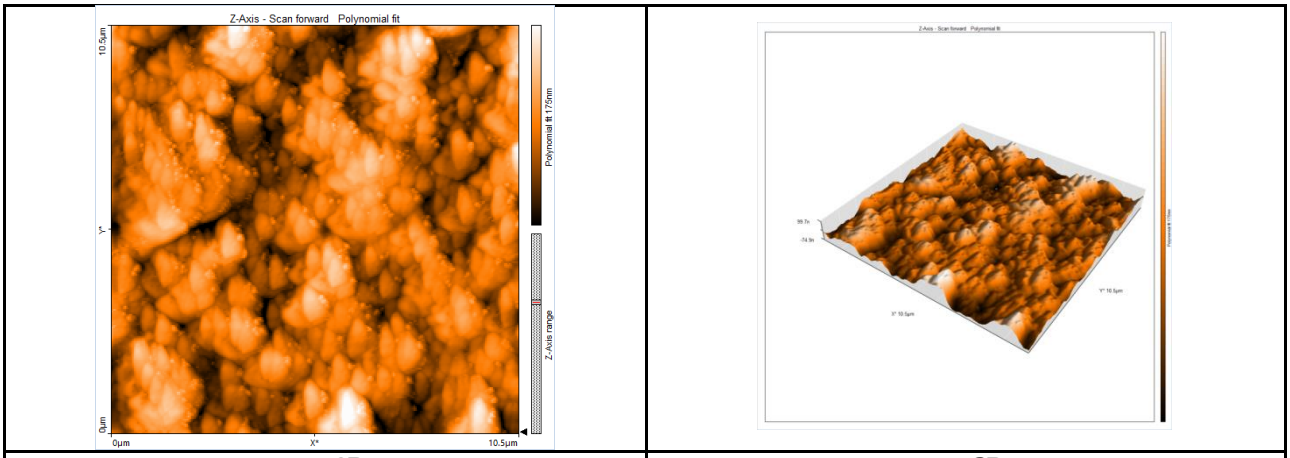

2D	3D
Sq (rms)= 38.34 nm	Sa= 30.17 nm

FIGURE 7 (a) Two-dimensional, and (b) three-dimensional atomic force microscopy topographic images of La_2O_3 thin film deposited by PLD

3.2 XRD

The XRD profile for the X-ray peaks of the La_2O_3 and FTO in Fig. 8 reveals diffraction peaks arising from both the La_2O_3 thin film and the underlying FTO substrate. The FTO layer, composed of fluorine-doped SnO_2 in a rutile tetragonal phase (JCPDS 41-1445, space group $P4_2/mnm$), exhibits its most intense peaks at $2\theta \approx 26.61°$ (110), 33.89° (101), 37.95° (200), 51.78° (211), 54.78° (220), 57.77° (002), 61.98° (310), 64.77° (112), and 78.65° (321). These reflections are evident in the pattern, particularly the sharp substrate-related peaks at ~26.6°, ~38°, ~51.8°, and ~54.8°.

Superimposed on these are the peaks corresponding to the hexagonal A-type La_2O_3 phase (JCPDS 05-0602, space group P-3m1) with characteristic reflections at $2\theta \approx 15.72°$ (100), 27.39° (002), 29.32° (101), 39.52° (102), 48.23° (110), 54.62° (103), 64.43° (112), and 76.98° (201). Several of these film peaks partially overlap with FTO substrate

peaks, for example: La_2O_3 (002) with FTO (110) near 26–27°, La_2O_3 (103) with FTO (220) near 54–55°, and La_2O_3 (112) with FTO (112) near 64–65°. The strong La_2O_3-specific peak at ~39.5° (102) is well resolved from substrate peaks and is a reliable indicator of the film phase.

The lattice parameters of the hexagonal La_2O_3 were calculated from Bragg's law, and the hexagonal plane spacing equation [18-21]:

$$\frac{1}{d_{hkl}^2} = \frac{4}{3}\frac{h^2+hk+k^2}{a^2} + \frac{l^2}{c^2} \quad (1)$$

The refined parameters are approximately a≈3.94 Å, c≈6.13 Å, with axial angles $\alpha=\beta=90^o$ and $\gamma=120^o$.

The sharpness of the La_2O_3 peaks confirms high crystallinity and phase purity, while the coexistence of substrate peaks indicates strong adhesion and epitaxial compatibility.

The interplanar spacing was determined from Bragg's law, [22]

$$n\lambda = 2d\sin\theta \Rightarrow d = \frac{\lambda}{2\sin\theta} \quad (2)$$

where n = 1, λ = 0.15406 nm for Cu Kα radiation, and θ is the Bragg angle. The crystallite size was estimated using the Scherrer equation, [23]

$$D = \frac{K\lambda}{\beta\cos\theta} \quad (3)$$

with K = 0.9, and β being the corrected FWHM in radians, calculated as [24]

$$\beta = \sqrt{\beta_{means}^2 - \beta_{inst}^2} \quad (4)$$

where βmeans is the measured peak width and βinst is the instrumental broadening. The dislocation density was obtained from, [25]

$$\delta = \frac{1}{D^2} \quad (5)$$

and the microstrain was evaluated using, [26]

$$\varepsilon = \frac{\beta}{4\tan\theta} \quad (6)$$

Reference standards JCPDS card No. 41-1445 for FTO and No. 05-0602 for La_2O_3 were used to identify the crystal phases.

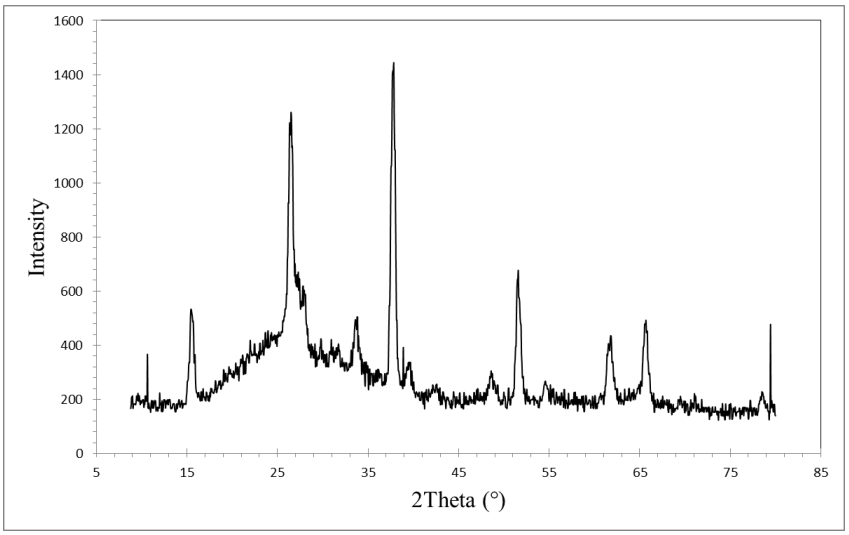

FIGURE 8 X-ray diffraction (XRD) pattern of La_2O_3 thin film deposited by PLD onto an FTO -coated glass substrate, showing Bragg reflections corresponding to both the film and the substrate

Table 1 summarizes the structural properties of the La_2O_3 thin film deposited by PLD on an FTO-coated glass substrate, as derived from the XRD analysis. The data include the measured diffraction angles (2θ), full width at half maximum (FWHM), corresponding Miller indices (hkl), calculated interplanar spacing (d), crystallite size (D), dislocation density (δ), and microstrain (ε) for each identified Bragg reflection of both the substrate and the thin film.

For the FTO substrate, the intense peaks at 2θ ≈ 26.61°, 33.89°, 37.95°, and 51.78° correspond to the (110), (101), (200), and (211) planes of tetragonal SnO_2, consistent with the JCPDS card No. 41-1445. These peaks exhibit relatively narrow FWHM values (0.22–0.34°), indicating large crystallite sizes (21–31 nm) and low dislocation densities, reflecting the high crystallinity of the commercial FTO coating. The average crystallite size for the FTO substrate is approximately 26.21 nm, with a mean dislocation density on the order of 1.45×1015 m−2, and a low average microstrain of 1.12×10^{-3} (dimensionless).

For the PLD-deposited La_2O_3 film, the diffraction peaks at 2θ ≈ 15.72°, 27.39°, 29.32°, 39.52°, 48.23°, 54.62°, 64.43°, and 76.98° are indexed to the (100), (002), (101), (102), (110), (103), (112), and (201) planes of the hexagonal A-type La_2O_3 phase (JCPDS card No. 05-0602). The calculated lattice parameters are approximately a=3.94 Å, and

c=6.13 Å, with space group P3¯m1, and the axial angles α = β = 90°, γ = 120°, confirming the trigonal symmetry of the structure. The La_2O_3 peaks are generally broader (FWHM 0.28–0.50°) than those of the substrate, corresponding to smaller crystallite sizes (16–23 nm), higher dislocation densities (≈3.0×1015 m^{-2}, and slightly higher microstrain levels (≈1.85×10^{-3}).

The reduced crystallite size and higher microstrain in La_2O_3 compared to FTO are typical for PLD-grown oxide films due to rapid quenching and high nucleation rates in the plasma plume. The results confirm that the film is polycrystalline with well-defined hexagonal La_2O_3 peaks, and the overlap with substrate peaks does not obscure the identification of the film phase. This high degree of crystallinity, combined with nanoscale grain size, suggests that the PLD process parameters used were effective in producing a uniform and structurally coherent La_2O_3 layer on the conductive FTO substrate.

Table 1 Structural parameters of La_2O_3 thin film deposited by PLD on an FTO-coated glass substrate, including diffraction angles (2θ), full width at half maximum (FWHM), Miller indices (hkl), interplanar spacing (d), crystallite size (D), dislocation density (δ), and microstrain (ε) for both substrate and film phases

Samples	2Theata	FWHM	hkl	d-Spacing (A)	D (nm)	δ (m)-2	ε
FTO thin film	26.61	0.22	-110	3.3472	41.66	5.76E+14	3.62E-03
	33.89	0.26	-101	2.643	34.6	8.35E+14	3.44E-03
	37.95	0.28	-200	2.369	32.12	9.69E+14	3.32E-03
	51.78	0.34	-211	1.7641	27.17	1.35E+15	2.92E-03
	54.78	0.36	-220	1.6744	25.87	1.49E+15	2.91E-03
	57.77	0.38	-2	1.5946	24.75	1.63E+15	2.90E-03
	61.98	0.40	-310	1.4961	23.93	1.75E+15	2.81E-03
	64.77	0.42	-112	1.4382	23.06	1.88E+15	2.81E-03
	78.65	0.50	-321	1.2155	20.96	2.28E+15	2.61E-03
	26.61	0.22	-110	3.3472	41.66	1.42E+15	3.04E-03
average					28.24	5.97E+14	**6.19E-03**
La_2O_3 thin film	15.72	0.22	-100	5.6328	40.93	1.02E+15	4.68E-03
	27.39	0.28	-2	3.2536	31.26	1.19E+15	4.72E-03
	29.32	0.30	-101	3.0437	29.03	1.58E+15	4.07E-03
	39.52	0.35	-102	2.2784	25.17	1.98E+15	3.78E-03
	48.23	0.40	-110	1.8854	22.47	2.08E+15	3.45E-03
	54.62	0.42	-103	1.6789	21.92	2.18E+15	3.04E-03
	64.43	0.45	-112	1.445	21.4	2.33E+15	2.69E-03
	76.98	0.50	-201	1.2377	20.72	1.62E+15	4.08E-03
average					26.61	5.76E+14	**3.62E-03**

Based on the current structural and optical results, transition-metal and rare-earth dopants would be most suitable for La_2O_3 because they can tune electronic and optical properties without compromising film stability.

- Transition-metal dopants (e.g., Cu, Co, Ni, Fe, or Mn): These elements introduce localized d-states near the conduction or valence bands, effectively narrowing the optical band gap and enhancing visible-light absorption. For instance, Cu or Co doping can shift the absorption edge toward longer wavelengths, useful for UV–visible photodetector or photocatalytic applications.
- Rare-earth dopants (e.g., Ce, Y, or Gd): Iso-valent substitution at the La^{3+} site can reduce lattice strain while improving dielectric properties and thermal stability. Such doping could enhance charge storage and high-k dielectric performance by modifying the local polarization environment.

Therefore, Cu- or Co-doped La_2O_3 would be ideal to tailor optical absorption, whereas Ce- or Y-doped La_2O_3 would benefit electronic and dielectric applications. The choice depends on the intended device function.

3.3 FTIR

Fig. 9 presents the Fourier Transform Infrared (FTIR) spectrum of the La_2O_3 thin film deposited on an FTO-coated glass substrate in the wavenumber range of 4000–500 cm^{-1}. The spectrum exhibits high transmittance (> 92 %) across most of the mid-infrared region, indicating the optical transparency of the film and the low absorption from organic residues.

No significant peaks are observed in the 3500–3000 cm^{-1} range, suggesting the absence of strong O–H stretching modes from adsorbed water or hydroxyl groups, which typically appear around ~3400 cm^{-1}. Similarly, the 3000–2800 cm^{-1} C–H stretching bands from organic contaminants are not evident, confirming the cleanliness of the film surface after deposition.

A small feature is observed near ~1384 cm^{-1}, which can be attributed to weak carbonate (CO_3^{2-}) bending vibrations, possibly due to minimal atmospheric CO_2 adsorption during sample handling. The broad, intense absorption band beginning around 900 cm^{-1} and extending to 500 cm^{-1} is characteristic of metal–oxygen stretching vibrations. For La_2O_3, the dominant La–O stretching mode generally appears in the range of 500–700 cm^{-1}, with a strong band centered near ~560 cm^{-1}, indicating the formation of La–O bonds in the hexagonal A-type La_2O_3 crystal lattice.

In addition, contributions from the underlying FTO substrate are expected in this low-wavenumber region. Sn–O and Sn–O–Sn lattice vibrations of SnO_2 appear in the 500–750 cm^{-1} range, often overlapping with La–O modes, leading to a composite absorption band. The absence of pronounced mid-IR absorption features confirms that the film is largely free of hydroxylated or carbonaceous species, and the strong metal–oxygen stretching region supports the successful formation of stoichiometric La_2O_3 on the conductive FTO surface.

Table 2 presents the main infrared absorption features detected in the FTIR spectrum of the La_2O_3 thin film and attributes each band to a specific vibrational mode and material phase. The high transmittance values and the absence of strong O–H and C–H bands confirm the chemical purity of the film, while the prominent La–O stretching modes between 600–520 cm^{-1} confirm the successful formation of La_2O_3. Bands related to the Sn–O vibrations of the FTO layer and the Si–O–Si stretching of the glass substrate are also identified, reflecting the multilayered structure of the sample.

Table 2 FTIR band assignments for La_2O_3 thin film on FTO-coated soda-lime glass

Wavenumber (cm^{-1})	Assignment (vibrational mode)	Origin (material)	Notes
~3400 (weak/absent)	O–H stretching (adsorbed H_2O / surface –OH)	La_2O_3 surface / ambient	Largely absent → low hydroxylation
~1630 (very weak/absent)	H–O–H bending (δ(H_2O))	Adsorbed moisture	Consistent with minimal water uptake
~1384 (very weak)	ν_3(CO_3^{2-}) asymmetric bending	Adventitious carbonates	From light CO_2 adsorption during handling
1100–1000 (broad drop in T)	Si–O–Si asymmetric stretching	Soda-lime glass substrate	Dominant substrate band; drives the strong transmittance decrease
810–780 (shoulder/weak)	Si–O–Si symmetric stretching / ring breathing	Soda-lime glass substrate	Often appears as a shoulder on glass
750–700 (weak to moderate)	Sn–O–Sn / Sn–O lattice modes	FTO (SnO_2, rutile)	Overlaps with glass/La–O tail; intensity depends on FTO thickness
650–600 (moderate)	Sn–O lattice vibration (Eu/A_{2u} IR-active modes)	FTO (SnO_2, rutile)	Frequently merges with La–O envelope below 650 cm^{-1}
600–520 (strong composite band)	La–O stretching in La–O–La network	La_2O_3 (hexagonal A-type)	Signature of La_2O_3; main film-related absorption in this region
~560 (local minimum in T)	La–O stretching (fundamental)	La_2O_3	Often used as a fingerprint for La_2O_3 formation
520–480 (tail)	La–O lattice / bending modes	La_2O_3	Lower-frequency tail of La–O envelope
<480 (edge of range)	External modes / multi-phonon background	La_2O_3 + substrate mixture	Typically outside measured window; appears as baseline roll-off

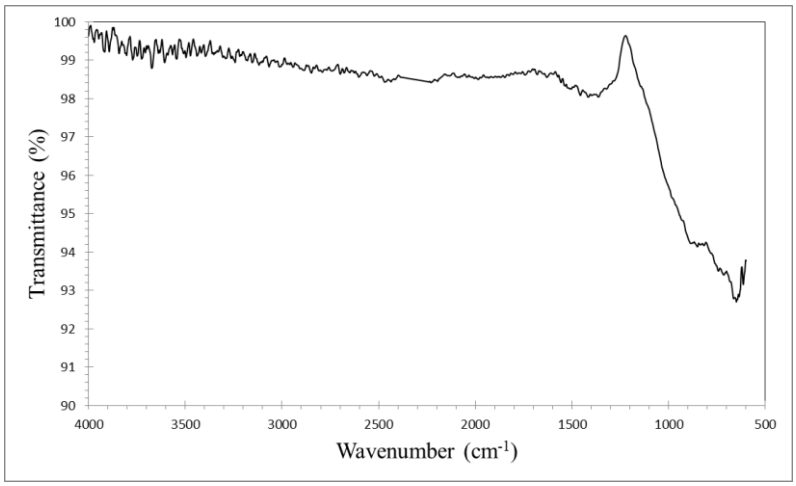

FIGURE 9 FTIR spectrum of La_2O_3 thin film deposited by PLD on an FTO-coated soda-lime glass substrate

3.4 Raman

Fig. 10 shows the Raman spectrum of the La_2O_3 thin film deposited by pulsed laser deposition (PLD) on an FTO-coated soda-lime glass substrate, measured in the range of 0–4000 cm^{-1}. The spectrum displays several broad and overlapping features, characteristic of polycrystalline thin films and compounded by the presence of both the La_2O_3 layer and the underlying FTO.

Table 3 presents the Raman band assignments for La_2O_3 thin film deposited by PLD on an FTO-coated soda-lime glass substrate. The table lists the observed Raman shifts, their corresponding vibrational modes, and the material origins, distinguishing between contributions from the La_2O_3 film and the FTO conductive layer.

In the low-wavenumber region (< 200 cm^{-1}), a strong band is observed, corresponding to lattice vibrations involving heavy La atoms in the hexagonal A-type La_2O_3 structure. Peaks in this range are typically assigned to Eg and A1g modes associated with La–O stretching and bending vibrations in the rare-earth oxide lattice.

A broader feature around ~400–700 cm^{-1} is attributed to La–O stretching modes in La_2O_3, overlapping with Sn–O vibrational modes from the FTO substrate (SnO_2 in rutile structure). SnO_2 is known to exhibit Raman-active modes such as Eg (~475 cm^{-1}), A1g (~632 cm^{-1}), and B2g (~774 cm^{-1}). The convolution of these modes with La–O vibrations produces a broad composite band in this region.

The weak feature between 900–1100 cm^{-1} may arise from overtones or defect-induced modes, while the gradually decreasing intensity beyond 1200 cm^{-1} indicates minimal contribution from high-frequency vibrations. No significant C–H (~2900 cm^{-1}) or O–H (~3400 cm^{-1}) stretches are observed, consistent with FTIR results that showed minimal contamination by hydroxyl or organic species.

The broad nature of the observed peaks suggests nanocrystalline domains and possible strain-induced peak broadening, consistent with the XRD and AFM findings.

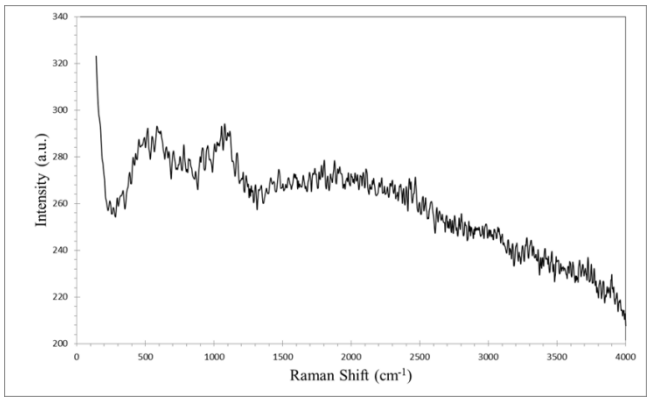

FIGURE 10 Raman spectrum of La_2O_3 thin film deposited by PLD on an FTO-coated soda-lime glass substrate, recorded in the range 0–4000 cm^{-1}

Table 3 Raman band assignments for La_2O_3 thin film on FTO-coated soda-lime glass

Raman Shift (cm^{-1})	Assignment (Mode)	Origin (Material)	Notes
<200	E_g, A1g lattice modes (La–O bending)	La_2O_3	Heavy La atom vibrations
~475	Eg mode (Sn–O stretching)	FTO (SnO_2)	Overlaps with La–O modes
~632	A1g mode (Sn–O symmetric stretching)	FTO (SnO_2)	Strong Raman-active mode
650–700	La–O stretching in La_2O_3 lattice	La_2O_3	May merge with Sn–O band
900–1100	Overtone/defect-related modes	La_2O_3 (possible)	Weak intensity
>3000	Broad background, possible multi-phonon scattering	La_2O_3 + substrate	No sharp OH/CH peaks

3.5 Optical Properties

Fig. 11 shows that the La_2O_3/FTO stack is highly transparent in the visible–NIR, with a broad plateau of ~72–75 % between ~420 and 1100 nm. The steep rise in T from ~2–5 % at 300 nm to ~65–70 % by ~380–400 nm reflects the fundamental absorption edge of the La_2O_3 layer; beyond this edge, extinction is minimal and the spectrum is dominated by transmission through the FTO-coated glass. The absence of pronounced interference fringes suggests an optically rough or thickness-nonuniform surface (consistent with AFM, Sa ≈ 30 nm), and/or a film thickness outside the strong-fringe regime for this wavelength window. A weak shoulder near ~700 nm likely arises from the substrate/overlayer optical stack rather than intrinsic electronic transitions.

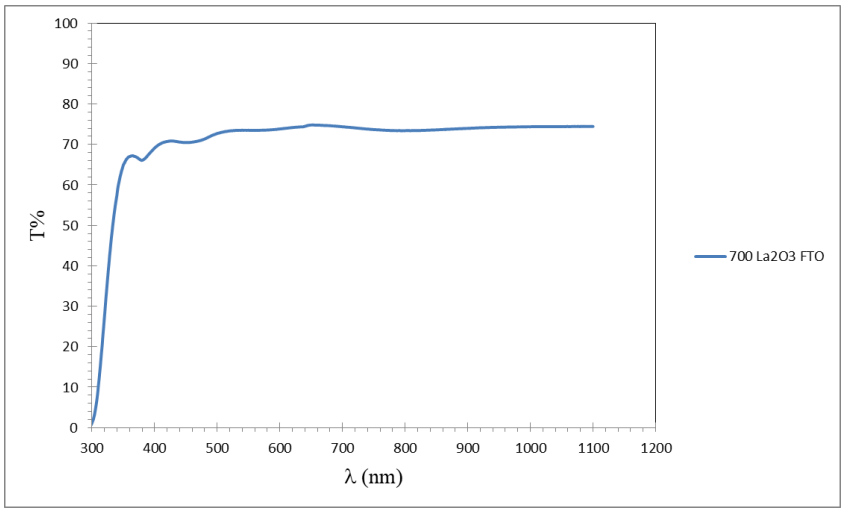

FIGURE 11 Optical transmittance (T%) of the La_2O_3 thin film deposited by PLD on FTO (700 mJ), recorded over 300–1100 nm

The spectrum in Fig. 12 reveals that the La_2O_3/FTO system exhibits strong absorption in the UV region with a sharp decrease in absorbance from ~1.9 at 300 nm to below 0.3 by ~360–380 nm. This sharp decline corresponds to the optical absorption edge, which reflects the onset of interband electronic transitions in La_2O_3. Beyond ~400 nm, the absorbance stabilizes at a very low value (~0.15), indicating high transparency in the visible and near-infrared regions, consistent with the transmittance results in Fig. 5.

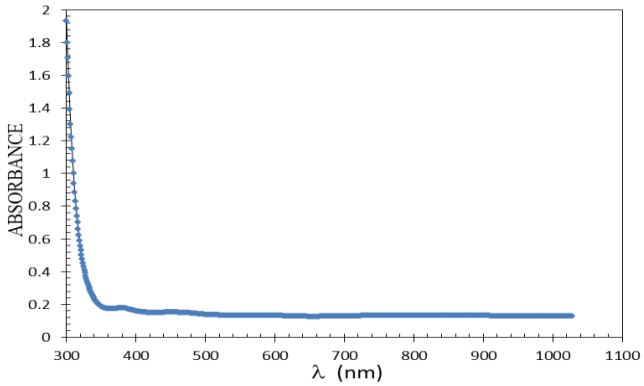

FIGURE 12 Optical absorbance spectrum of La_2O_3 thin film deposited by PLD at 700 mJ on an FTO-coated soda-lime glass substrate, measured over 300–1100 nm

Fig. 13 presents the variation of the optical absorption coefficient (α) of the La_2O_3 thin film deposited by PLD at 700 mJ on an FTO-coated soda-lime glass substrate, across the wavelength range of 300–1100 nm. The absorption coefficient α was calculated from the absorbance spectrum using the relation [27]:

$$\alpha = \frac{2.303\ A}{d} \quad (7)$$

where A is the absorbance and d is the film thickness. The spectrum shows a very high α value exceeding 2.1×10^5 cm^{-1} at 300 nm, indicative of strong electronic transitions in the UV range. This high absorption in the short-wavelength region confirms the direct allowed nature of the band-to-band transitions in La_2O_3.

As the wavelength increases beyond ~380 nm, α decreases sharply and stabilizes at ~1.5×10^4 cm^{-1} across the visible and near-infrared regions. Such low absorption values in the visible range are consistent with the high transmittance (Fig. 11) and low absorbance (Fig. 13), demonstrating the optical transparency of the film.

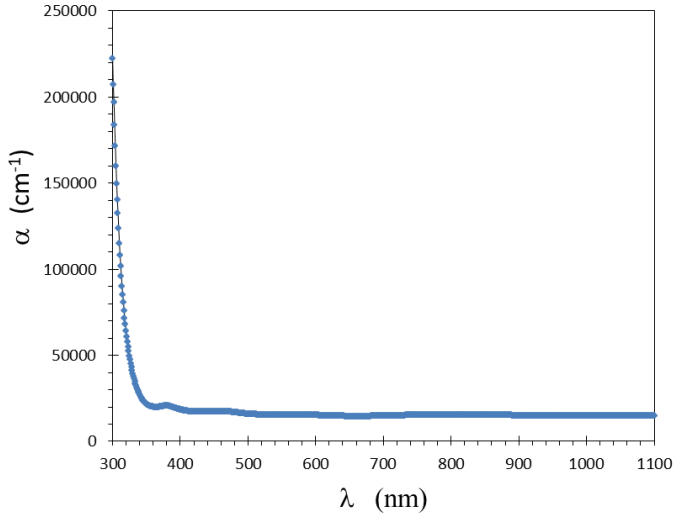

FIGURE 13 Optical absorption coefficient (α) spectrum of La_2O_3 thin film deposited by PLD at 700 mJ on an FTO-coated soda-lime glass substrate, measured in the wavelength range of 300–1100 nm

The extinction coefficient (k) for the thin film can be found from the absorption coefficient (α) via this equation

$$k=\alpha\lambda/4\pi \quad (8)$$

Fig. 14 presents the spectral dependence of the extinction coefficient (k) for the La_2O_3 thin film deposited by PLD at 700 mJ on an FTO-coated soda-lime glass substrate, over the wavelength range of 300–1100 nm. The extinction coefficient exhibits a maximum of approximately 5.0×10^{-13} at 300 nm, corresponding to strong photon absorption near the fundamental edge. As the wavelength increases, *k* rapidly decreases and stabilizes at about 1.0×10^{-13} in the visible region, confirming low optical losses and high transparency.

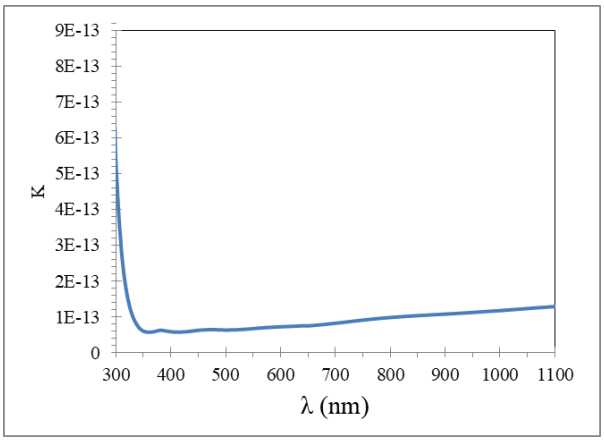

FIGURE 14 Extinction coefficient (k) of the La_2O_3 thin film deposited by PLD at 700 mJ on an FTO-coated glass substrate as a function of wavelength (300–1100 nm), showing high UV absorption with low attenuation in the visible region, indicative of good optical transparency

Fig. 15 presents the Tauc plot $(\alpha h\nu)^2$ as a function of photon energy ($h\nu$) for the La_2O_3 thin film deposited by pulsed laser deposition (PLD) at 700 mJ on an FTO-coated glass substrate. The optical band gap can then be obtained from a Tauc analysis for a direct allowed transition, [28]

$$(\alpha h\nu)^2 = A\,(h\nu - Eg) \quad (9)$$

by extrapolating the linear portion of $(\alpha h\nu)^2$ versus $h\nu$ to zero, yielding $Eg\approx3.81$ eV for this film. The relatively high visible transmittance with a UV-edge near ~325–340 nm indicates that the PLD-grown La_2O_3 acts as a wide-band-gap, low-loss overlayer on FTO, suitable for transparent electronics, UV photonics, and window/buffer roles in optoelectronic stacks.

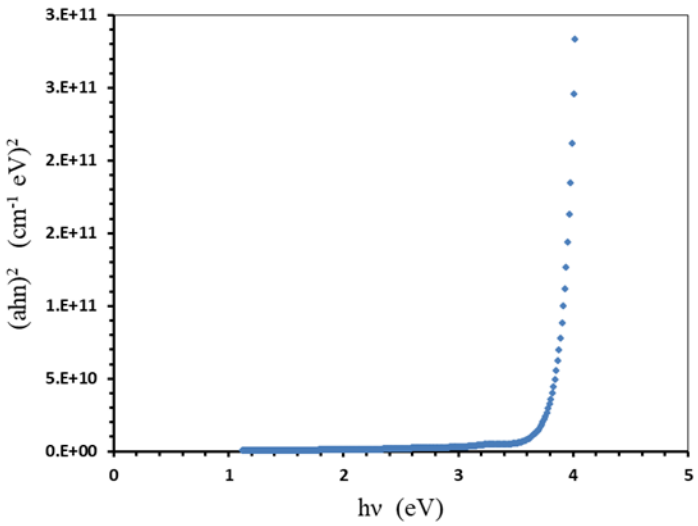

FIGURE 15 Tauc plot $(\alpha h\nu)^2$ versus photon energy (hν) for the La_2O_3 thin film deposited by PLD at 700 mJ on an FTO-coated glass substrate, showing a direct allowed optical transition

4. Conclusions

This study successfully demonstrated the fabrication of high-quality La_2O_3 thin films using the pulsed laser deposition (PLD) technique under controlled conditions, achieving films with excellent crystallinity, uniform surface morphology, and high optical transparency. By integrating XRD, AFM, FTIR, Raman, and UV–Vis analyses, the work provided a comprehensive understanding of the structural and optical behavior of La_2O_3 films on FTO substrates. The identification of a hexagonal crystalline phase, uniform nanograin distribution, and a wide direct band gap of 3.81 eV confirms that the films possess the necessary attributes for ultraviolet (UV) and transparent electronic applications.

Beyond confirming film quality, this investigation emphasizes the versatility of PLD in producing stoichiometric, adherent, and optically efficient La_2O_3 layers suitable for integration into optoelectronic devices. The correlation established between morphology, crystallinity, and optical performance offers valuable insight into how deposition parameters influence film quality — an important foundation for tailoring material functionality in high-k dielectric and UV photonic systems. Nevertheless, the study also highlights current limitations, particularly the absence of electrical characterization and the lack of parameter optimization. Addressing these aspects through systematic variation of laser fluence, substrate temperature, and ambient oxygen pressure could further enhance film performance. Future work should also explore doping strategies with transition metals or rare-earth elements (such as Cu, Co, or Ce) to tune optical and electronic properties, alongside post-annealing treatments to improve phase stability.

FUNDING

None

ACKNOWLEDGEMENT

The authors would like to thank the anonymous reviewers for their efforts.

CONFLICTS OF INTEREST

The authors declare no conflict of interest

REFERENCES

[1] Y.-Y. Lee, B. Sriram, S.-F. Wang, Sakthivel Kogularasu, and Guo-Ping Chang-Chien, "A comprehensive review on emerging role of rare earth oxides in electrochemical biosensors," *Microchemical journal*, vol. 193, pp. 109140–109140, Oct. 2023, doi: https://doi.org/10.1016/j.microc.2023.109140.

[2] A. Bhattacharya *et al.*, "THz carrier dynamics in SrTiO3/LaTiO3 interface two-dimensional electron gases," *arXiv (Cornell University)*, Mar. 2025, doi: https://doi.org/10.48550/arxiv.2503.21341.

[3] P. Banerjee and K. Mukhopadhyay, "Electronic, magnetic and optical properties of transition metal doped Nd2O3: A DFT insight," *Computational and Theoretical Chemistry*, vol. 1220, pp. 114016–114016, Jan. 2023, doi: https://doi.org/10.1016/j.comptc.2022.114016.

[4] J. Liu *et al.*, "Application of Solution-Processed High-Entropy Metal Oxide Dielectric Layers with High Dielectric Constant and Wide Bandgap in Thin-Film Transistors," *Micromachines*, vol. 15, no. 12, pp. 1465–1465, Nov. 2024, doi: https://doi.org/10.3390/mi15121465.

[5] Matteo Beggiato *et al.*, "Detection of crystalline defects in Si/SiGe superlattices towards 3D-DRAM applications," Apr. 2024, doi: https://doi.org/10.1117/12.3011279.

[6] A. Sawka, "Nanocrystalline Lanthanum Oxide Layers on Tubes Synthesized Using the Metalorganic Chemical Vapor Deposition Technique," *Materials*, vol. 17, no. 22, p. 5539, Nov. 2024, doi: https://doi.org/10.3390/ma17225539.

[7] A. Herrmann *et al.*, "The effect of glass structure and local rare earth site symmetry on the optical properties of rare earth doped alkaline earth aluminosilicate glasses," *Acta Materialia*, vol. 249, pp. 118811–118811, Feb. 2023, doi: https://doi.org/10.1016/j.actamat.2023.118811.

[8] M. Wang, "Technology of High-k/Metal-Gate Stack," *Journal of Physics: Conference Series*, vol. 2798, no. 1, p. 012039, Jul. 2024, doi: https://doi.org/10.1088/1742-6596/2798/1/012039.

[9] M. M. Alkhamisi, A. F. Qasrawi, and H. K. Khanfar, "Growth and Characterization of Lanthanum Germanide Thin Films by the Thermal Evaporation Technique," *Crystal Research and Technology*, vol. 58, no. 9, Jun. 2023, doi: https://doi.org/10.1002/crat.202300049.

[10] Mokhtar Hjiri, Anouar Jbeli, Nouf Ahmed Althumairi, N. Mustapha, and A. M. Aldukhayel, "Ceramic perovskites via sol–gel processing: progress, challenges, and applications," *Journal of Sol-Gel Science and Technology*, Sep. 2025, doi: https://doi.org/10.1007/s10971-025-06948-6.

[11] S. R. Pilli *et al.*, "The effect of Ar:O_2 gas ratios on the structural and optical properties of RF sputter-deposited La_2O_3-doped ZnO thin films," *Semiconductor Science and Technology*, vol. 38, no. 11, pp. 115006–115006, Sep. 2023, doi: https://doi.org/10.1088/1361-6641/acfe91.

[12] S. R. Patil, V. N. Barhate, V. S. Patil, K. S. Agrawal, and A. M. Mahajan, "The effect of post-deposition annealing on the chemical, structural and electrical properties of Al/ZrO2/La2O3/ZrO2/Al high-k nanolaminated MIM capacitors," *Journal of Materials Science Materials in Electronics*, vol. 33, no. 14, pp. 11227–11235, Apr. 2022, doi: https://doi.org/10.1007/s10854-022-08097-w.

[13] V. N. Barhate, K. S. Agrawal, V. S. Patil, and A. M. Mahajan, "Post-deposition-annealed lanthanum-doped cerium oxide thin films: structural and electrical properties," *Rare Metals*, vol. 40, no. 7, pp. 1835–1843, Apr. 2020, doi: https://doi.org/10.1007/s12598-020-01380-x.

[14] N. A. Shepelin, Z. P. Tehrani, N. Ohannessian, C. W. Schneider, D. Pergolesi, and T. Lippert, "A practical guide to pulsed laser deposition," *Chemical Society Reviews*, vol. 52, no. 7, pp. 2294–2321, 2023, doi: https://doi.org/10.1039/d2cs00938b.

[15] P. Mandal, U. P. Singh, and S. Roy, "A Review on the effects of PVD RF sputtering parameters on rare earth oxide thin films and their applications," *IOP Conference Series Materials Science and Engineering*, vol. 1166, no. 1, pp. 012022–012022, Jul. 2021, doi: https://doi.org/10.1088/1757-899x/1166/1/012022.

[16] J. Yu, W. Han, Abdulsalam Aji Suleiman, S. Han, N. Miao, and Francis Chi-Chung Ling, "Recent Advances on Pulsed Laser Deposition of Large-Scale Thin Films," *Small methods*, Dec. 2023, doi: https://doi.org/10.1002/smtd.202301282.

[17] M. M. El-shabaan, A. Mohamed, M. I. Youssif, N. A. El-Ghamaz, and E. M. Ahmed, "Comparative study on the influence of rare earth ion doping on the structural and optical properties of simple B2O3–Na2O glasses," *Scientific Reports*, vol. 15, no. 1, Oct. 2025, doi: https://doi.org/10.1038/s41598-025-21224-x.

[18] M. A. Awad, A. M. Rayan, I. A. Abdel-Latif, and M. R. Ahmed, "Temperature induced structural distortion and their effect on the physical properties of La0.6Sr0.4Mn0.8Co0.2O3 nanoparticles," *Scientific Reports*, vol. 15, no. 1, Aug. 2025, doi: https://doi.org/10.1038/s41598-025-14101-0.

[19] A. M. Enad and J. M. Rzaij, "Fabrication and characterization of CuO/La_2O_3 nanocomposite thin films by pulsed laser deposition for optoelectronic applications," Sci. J. Phys. Appl. Sci., vol. 7, no. 2, pp. 45–53, 2025, https://doi.org/10.54153/sjpas.2025.v7i2.1123.

[20] Shashi Priya Balmuchu, Ethireddy Radhika, and Pamu Dobbidi, "The impact of oxygen partial pressure in modifying energy storage property of lanthanum doped multiferroic bismuth ferrite thin films deposited via pulsed laser deposition," *Journal of Energy Storage*, vol. 71, pp. 108179–108179, Jun. 2023, doi: https://doi.org/10.1016/j.est.2023.108179.

[21] M. Enneffati, M. Rasheed, B. Louati, K. Guidara, and R. Barillé, "Morphology, UV–visible and ellipsometric studies of sodium lithium orthovanadate," Optical and Quantum Electronics, vol. 51, no. 9, Aug. 2019, doi: https://doi.org/10.1007/s11082-019-2015-5.

[22] M. Rasheed and R. Barillé, "Comparison the optical properties for Bi2O3 and NiO ultrathin films deposited on different substrates by DC sputtering technique for transparent electronics," Journal of Alloys and Compounds, vol. 728, pp. 1186–1198, Dec. 2017, doi: https://doi.org/10.1016/j.jallcom.2017.09.084.

[23] T. Saidani, M. Zaabat, M. S. Aida, R. Barille, M. Rasheed, and Y. Almohamed, "Influence of precursor source on sol–gel deposited ZnO thin films properties," Journal of Materials Science: Materials in Electronics, vol. 28, no. 13, pp. 9252–9257, Mar. 2017, doi: https://doi.org/10.1007/s10854-017-6660-9.

[24] E. Kadri, M. Krichen, R. Mohammed, A. Zouari, and K. Khirouni, "Electrical transport mechanisms in amorphous silicon/crystalline silicon germanium heterojunction solar cell: impact of passivation layer in conversion efficiency," Optical and Quantum Electronics, vol. 48, no. 12, Nov. 2016, doi: https://doi.org/10.1007/s11082-016-0812-7.

[25] A. Aukštuolis et al., "Measurement of charge carrier mobility in perovskite nanowire films by photo-celiv method," Proceedings of the Romanian Academy Series A - Mathematics Physics Technical Sciences Information Science, vol. 18, no. 1, pp. 34–41, 2017, Available: https://hal.archives-ouvertes.fr/hal-02443179.

[26] R. S. Mahmood et al., "Leveraging normal distribution and fuzzy S-function approaches for solar cell electrical characteristic optimization," Journal of the Mechanical Behavior of Materials, vol. 34, no. 1, Jan. 2025, doi: https://doi.org/10.1515/jmbm-2025-0040.

[27] Areej Adnan Hateef, Essebti Dhahri, M. Rasheed, Habiba Kadhim, Z. Abbas, and N. Hassan, "Study of the influence concentration difference of copper in properties of cerium nanopowder," Physics and Chemistry of Solid State, vol. 25, no. 4, pp. 801–810, Dec. 2024, doi: https://doi.org/10.15330/pcss.25.4.801-810.

[28] Kherifi Djelel, Ahcen Keziz, M. Rasheed, and Abderrazek Oueslati, "SiO2's influence on the dielectric properties of natural fluorapatite-derived bio-compounds," Ceramics International, Dec. 2024, doi: https://doi.org/10.1016/j.ceramint.2024.12.296.